



A Semi-analytical Model of Maximal First Principal Stress at Mode I Crack Tip

Simiao Yu¹ · Lixun Cai²

Received: 1 December 2023 / Revised: 23 April 2024 / Accepted: 23 April 2024
© The Chinese Society of Theoretical and Applied Mechanics 2024

Abstract

The first principal stress plays a key role in ductile fracture processes. Investigation of the distribution and evolution of the first principal stress at the crack tip is essential for exploring elastoplastic fracture behaviors. A semi-analytical model was developed in this study to determine the maximal first principal stress at the mode I crack tip with 3D constraints for materials following the Ramberg–Osgood law. The model, based on energy density equivalence and dimensional analysis, was validated through finite element analysis (FEA) of various materials and geometric dimensions of specimens with mode I cracks, under over 100 different types of working conditions. The dimensionless curves of maximal first principal stress versus load, as predicted by the model, agreed well with the FEA results, demonstrating the accuracy and applicability of the model. This research can provide a basis for future theoretical predictions of crack initiation and propagation.

Keywords Mode I crack · 3D constraints · Ramberg–Osgood law · Energy density equivalence · First principal stress

1 Introduction

Under the effects of manufacturing methods, damage, and other factors, structures in aerospace, nuclear power, chemical, and other engineering sectors frequently exhibit defects and cracks that can significantly impact the safety of systems. Investigation of fracture mechanical behaviors of cracked structures plays a key role in structural integrity analysis. To comprehend structural fractures, first crack tip stress field and deformation distribution should be understood.

Characterization of crack tip stress distribution has been an active research topic. In 1939, Westergaard [1] first described biaxial stress fields in internal cracks of a pressurized cylinder, which is considered as one of the earliest and most well-known methods to comprehend stress fields in cracked structures. In 1957, Williams [2] demonstrated that stress fields around crack tips in isotropic elastic materials could be represented as an infinite series. Since then, the Williams

series expansion has been the most popular analytical technique for modeling the mechanical field around crack tip in a planar domain. The first two components of the Williams series expansion denote stress intensity [3, 4] and T-stress [5] factors, respectively. For each cracked structure, the coefficient sequence in the Williams series expansion depends on the existing loading system and geometry. In addition, higher-order stress terms significantly affect the engineering description of stress fields for different fractured specimens [6]. In 2013, Berto and Lazzarin [7] derived an equation series to precisely define crack tip stress components, while the accuracy of complete stress fields in front of crack tips was unsatisfactory. In 2016, Larisa and Pavel [8] analytically determined stress expansion coefficients at crack tips for two collinear finite cracks with similar lengths in an infinite plane medium. Their study particularly focused on the effect of varying numbers of series expansion terms on stress distribution. The primary application of the Williams series expansion is in linear elastic fracture mechanics, and the analytical calculation of crack tip stress expansion coefficients remains an area deserving of in-depth studies.

Cherepanov [9] and Rice [10] independently proposed the *J*-integral for elastic–plastic fracture mechanics, an energy line integral demonstrating path independence for every contour surrounding the crack tip to characterize the crack-tip

✉ Lixun Cai
lix_cai@263.net

¹ School of Architecture and Civil Engineering, Xihua University, Chengdu 610039, China

² Applied Mechanics and Structure Safety Key Laboratory of Sichuan Province, School of Mechanics and Aerospace Engineering, Southwest Jiaotong University, Chengdu 610031, China

stress field intensity. In order to tackle the power-law plasticity problem of mode I cracks under plane conditions, Hutchinson [11] and Rice and Rosengren [12] presented the crack tip stress and strain field (HRR field) characterized by the J -integral in 1968. It has been proved that the J -integral uniquely determines crack tip stress and strain field strength. The proposed HRR field is a milestone in investigating crack tip stress and strain fields. Recent theoretical, experimental, and numerical analyses have revealed that the HRR field could accurately capture the inherent stress and strain properties in an annular region at the crack tip. The control region of the HRR field varies with the geometric configuration and size of the specimen. In general, the stress and strain field with high constraints under plane strain conditions can be effectively described by the HRR field.

For low-constrained cracked specimens under plane strain conditions, J - Q [13–15], J - A_2 [16, 17], and J - A [18–20] theories have been developed to describe the crack tip field. According to O’Dowd and Shih et al. [13–15], the J - Q theory offers a two-term crack tip field solution capable of accurately predicting stress fields under a wide spectrum of conditions ranging from small yield to large yield or pure plasticity. However, as an empirical parameter, Q depends on finite element calculations for specific materials or configurations, as well as the distance and angle between a chosen reference point and the crack tip. Yang and Chao et al. [16, 17] developed the J - A_2 theory on the basis of three asymptotic expansions of the crack tip stress field. Later, using a similar method, Nikishkov and Matvienko [18–20] developed a new version of the J - A theory, which was almost identical to the J - A_2 theory. Under some circumstances, constraint parameters such as Q , A_2 , A , or others could be transformed into one another, and their descriptive capabilities are comparable. For cracked specimens with different constraints and materials, the constraint parameters had to be separately determined by finite element calculations and could not be expressed analytically.

In recent years, many researchers have explored new methods to characterize crack tip stress fields. Withers [21] found that tomographic imaging and synchrotron X-ray diffraction could capture crack initiation and growth at 3D crack tips. The quantitative information of fracture mechanics regarding the area around the crack tip, such as fracture strength factor and stress field, could be retrieved to monitor crack tip fracture behavior. Sutton et al. [22] applied digital image correlation (DIC) to examine 3D effects near crack tips. Srilakshmi et al. [23] investigated crack growth in composite patch-repaired aluminum panels under fatigue loading using finite element analysis (FEA) and DIC. However, further development is needed to fully leverage these technologies for studying stress fields at crack tips.

Existing equations for stress and strain fields mainly focus on plane conditions, while cracked problems under 3D

constraints have rarely been studied. The paucity of comprehensive research on complex constraint conditions at crack tips is also a significant factor limiting our ability to predict crack initiation. It is essential to develop methods for analytically characterizing crack tip stress under 3D constraint conditions, which can not only depict stress characteristics but also effectively combine ductile fracture criteria with crack initiation studies, to lay a theoretical foundation for predicting crack structure and fracture behavior.

Previous research on critical ductile fracture criteria [24, 25] considered the critical first principal stress as the primary control parameter for ductile fractures. In this research, a semi-analytical model of critical first principal stress at the crack tip was developed using energy density equivalence and dimensional analysis, and the model’s accuracy was validated through FEA of different materials and geometric dimensions of specimens with mode I cracks.

2 Load–Displacement Model for Specimens with Mode I Cracks

2.1 Energy Density Equivalence

Uniaxial equivalent stress–strain relationships of representative volume elements (RVEs) are fundamental in continuum mechanics. In elastic–plastic fracture mechanics, the Ramberg–Osgood (R–O) law is commonly used to characterize constitutive relationships of materials under quasi-static conditions, which is stated as

$$\begin{cases} \varepsilon_{\text{eq}} = \varepsilon_{\text{e-eq}} + \varepsilon_{\text{p-eq}} \\ \varepsilon_{\text{e-eq}} = \frac{\sigma_{\text{eq}}}{E} \\ \varepsilon_{\text{p-eq}} = \left(\frac{\sigma_{\text{eq}}}{K}\right)^n \end{cases} \quad (1)$$

where $\varepsilon_{\text{p-eq}}$ and $\varepsilon_{\text{e-eq}}$ are the equivalent plastic and elastic strains, respectively; σ_{eq} and ε_{eq} are total equivalent stress and strain, respectively; K is stress strength coefficient in terms of MPa; E is elastic modulus in terms of GPa; and n is strain hardening exponent, which is a dimensionless parameter.

According to Chen and Cai [26–28], for any loaded specimens, the effective deformation region has a median energy density point, and the RVE strain energy density at this point is equal to the ratio of the specimen’s total strain energy to the effective deformation volume, i.e., the average strain energy. Based on the von Mises equivalence principle, the RVE strain energy density at a medium point subjected to complex stress states is also equal to that of the RVE under uniaxial equivalent stress states. This allows for a semi-analytical link between strain energy and material constitutive relation

parameters, geometric sizes, and the load or displacement of loaded specimens.

In the case of homogeneous and isotropic materials, the strain energy U of a loaded specimen can be stated as

$$U = \iiint_{\Omega} \mu(x, y, z) dV \tag{2}$$

where Ω is the effective deformation region of the loaded specimen, and $\mu(x, y, z)$ is the RVE strain energy density at any point in Ω .

On the basis of integral mean value theorem, there must be a point $M(x_M, y_M, z_M)$ in Ω at which the relationship between strain energy density μ_M and total strain energy U can be expressed as

$$\mu_M(x_M, y_M, z_M) = \frac{U}{V_{\text{eff}}} \tag{3}$$

where V_{eff} is the volume of effective deformation region of the specimen.

For the RVE at the medium point, there is

$$\mu_M = \int_0^{\varepsilon_{ij-M}} \sigma_{ij} d\varepsilon_{ij} = \int_0^{\varepsilon_{\text{eq-M}}} \sigma_{\text{eq}} d\varepsilon_{\text{eq}} \tag{4}$$

where σ_{ij} and ε_{ij} are stress and strain tensors under complex stress states, and $\varepsilon_{\text{eq-M}}$ and ε_{ij-M} are equivalent strain and strain tensor under certain deformation conditions, respectively.

According to Eqs. (2) and (4), the effective deformation region strain energy for a loaded specimen is stated as

$$U = \mu_M V_{\text{eff}} = V_{\text{eff}} \int_0^{\varepsilon_{\text{eq-M}}} \sigma_{\text{eq}} d\varepsilon_{\text{eq}} \tag{5}$$

If the uniaxial equivalent constitutive relation of the material can be described as $\sigma_{\text{eq}} = f(\varepsilon_{\text{eq}}, E, K, n)$, the relationship between $\varepsilon_{\text{eq-M}}$ and dimensionless displacement $\frac{v}{v^*}$ on the loaded line (with v^* being the characteristic displacement of the specimen) can be stated as $\varepsilon_{\text{eq-M}} = \phi \frac{v}{v^*}$, and that between $\frac{v}{v^*}$ and the volume of dimensionless effective deformation region V_{eff}/V^* (with V^* being the characteristic volume of the specimen) can be expressed as $V_{\text{eff}}/V^* = \varphi \frac{v}{v^*}$, the analytical description of the strain energy U of the loaded specimen can be obtained based on Eq. (5) as

$$U = V^* \varphi \left(\frac{v}{v^*} \right) \int_0^{\phi \left(\frac{v}{v^*} \right)} f(\varepsilon_{\text{eq}}, E, K, n) d\varepsilon_{\text{eq}} \tag{6}$$

The link between strain energy, material constitutive parameters, geometric sizes, and load or displacement on the load line can be precisely calculated after identifying the specific forms of functions f , ϕ , and φ .

2.2 3D Constraint Function of Specimens with Mode I Cracks

For specimens with mode I cracks under 3D constraints, the geometric dimension $\{L\}$ consists of the width W , crack length a , and thickness B ; denoted as $\{L\} = \{W, a, B\}$. Chen and Cai [26–28] developed an independent power law function relationship for dimensionless displacement v/v^* on the loading line and dimensionless effective deformation volume \bar{V}_{eff} for specimens with different geometric configurations. Therefore, the dimensionless effective deformation volume \bar{V}_{eff} for specimens with mode I cracks can be described as a separation relationship between dimensionless displacement function and dimensionless geometric function. This separation relationship is expressed as

$$\bar{V}_{\text{eff}} = \varphi(\{\bar{L}\}, \bar{v}) = G\left(\frac{a}{W}, \frac{B}{W}\right) \left[k_{01} \left(\frac{v}{v^*} \right)^{k_2} \right] \tag{7}$$

where v^* is the characteristic displacement of the specimen (equal to W for specimens with mode I cracks), k_{01} is the effective volume coefficient associated with geometric sizes, and k_2 is the effective volume exponent associated with specimen deformation.

$(1 - a/W)^{m_1}$ parameters suggested by Landes et al. [29] were utilized to further break down the dimensionless geometric function $G(a/W, B/W)$ as

$$G\left(\frac{a}{W}, \frac{B}{W}\right) = k_{02} \left(1 - \frac{a}{W}\right)^{m_1} g\left(\frac{B}{W}\right) \tag{8}$$

where $g(B/W)$ is the dimensionless thickness separation function, and k_{02} and m_1 are the effective volume reduction coefficient and index, respectively.

To address the effective deformation volume analysis of specimens with mode I cracks across a broad thickness range, $g(B/W)$ is anticipated as

$$g\left(\frac{B}{W}\right) = k_{03} \left[\arctan\left(b_1 \frac{B}{W}\right) + b_2 \right]^{m_2} \tag{9}$$

where b_1 and b_2 are thickness coefficients, and k_{03} and m_2 are the effective volume reduction coefficient and index, respectively.

Substitution of Eqs. (8) and (9) into Eq. (7) yields the dimensionless effective deformation volume \bar{V}_{eff} for specimens with mode I cracks as

$$\bar{V}_{\text{eff}} = \frac{V_{\text{eff}}}{W^2 B} = k_1 \left(1 - \frac{a}{W}\right)^{m_1} \left[\arctan\left(b_1 \frac{B}{W}\right) + b_2 \right]^{m_2} \left(\frac{v}{v^*}\right)^{k_2} \quad (10)$$

where k_1 is a constant only associated with specimen geometry, and $k_1 = k_{01}k_{02}k_{03}$.

The characteristic volume V^* is expressed as

$$V^* = W^2 B \left(1 - \frac{a}{W}\right)^{m_1} \left[\arctan\left(b_1 \frac{B}{W}\right) + b_2 \right]^{m_2} \quad (11)$$

Thus, from Eqs. (10) and (11), it can be inferred that

$$\phi\left(\frac{v}{v^*}\right) = \frac{V_{\text{eff}}}{V^*} = k_1 \left(\frac{v}{v^*}\right)^{k_2} \quad (12)$$

where all undetermined constants $k_1, k_2, m_1, m_2, b_1,$ and b_2 can be calculated using a small amount of FEA.

Based on Eqs. (6) and (12), the analytical function of strain energy for specimens with mode I cracks under 3D constraints can be written as

$$\begin{cases} U = V^* k_1 \left(\frac{v}{v^*}\right)^{k_2} \int_0^{\phi\left(\frac{v}{v^*}\right)} f(\varepsilon_{\text{eq}}, E, K, N) d\varepsilon_{\text{eq}} \\ V^* = W^2 B \left(1 - \frac{a}{W}\right)^{m_1} \left[\arctan\left(b_1 \frac{B}{W}\right) + b_2 \right]^{m_2} \end{cases} \quad (13)$$

2.3 Plastic Load–Displacement Semi-analytical Model for Specimens with Mode I Cracks

In specimens with mode I cracks under 3D constraints, only pure plastic deformation was considered. According to the R–O law, the material constitutive function f in Eq. (6) can be expressed as

$$\sigma_{\text{eq}} = f(\varepsilon_{\text{eq}}, E, K, n) = K \varepsilon_{\text{p-eq}}^{1/n} \quad (14)$$

Substitution of Eq. (14) into Eq. (13) yields the plastic strain energy U_p for specimens with mode I cracks as

$$U_p = \frac{nK V^*}{n+1} k_1 \left(\frac{v_p}{v^*}\right)^{k_2} \left[\phi\left(\frac{v_p}{v^*}\right) \right]^{1+1/n} \quad (15)$$

where v_p is the plastic displacement on the loading line. Referring to [26–28], the function ϕ is defined as

$$\phi\left(\frac{v}{v^*}\right) = k_3 \left(\frac{v_p}{v^*}\right)^{k_4} \quad (16)$$

where k_3 and k_4 are the effective strain coefficient and index under pure plastic conditions, respectively.

Substitution of Eq. (16) into Eq. (15) yields

$$\begin{cases} \frac{U_p}{U^*} = \xi_p \left(\frac{v_p}{v^*}\right)^{m_p+1} \\ \begin{cases} U^* = K V^* = K W^2 B \left(1 - \frac{a}{W}\right)^{m_1} \\ \quad \left[\arctan\left(b_1 \frac{B}{W}\right) + b_2 \right]^{m_2} \\ v^* = W \\ \xi_p = \frac{n k_1 k_3^{1/n+1}}{n+1} \\ m_p = \frac{k_4}{n} + k_4 + k_2 - 1 \end{cases} \end{cases} \quad (17)$$

where U^* is the characteristic strain energy function associated with specimen geometry, ξ_p is the curvature of the plastic energy–displacement curve, and m_p is the plastic deformation index.

Under quasi-static plastic conditions and following the functional principle, U_p is determined as

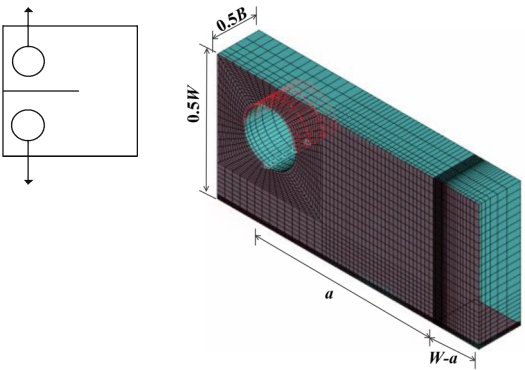
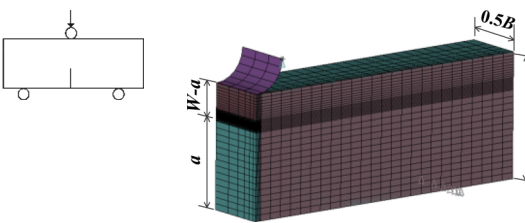
$$U_p = W \int_0^{v_p} P dv \quad (18)$$

Substituting Eq. (17) into Eq. (18), the derivatives of Eq. (18) with respect to v_p are obtained as

$$\begin{cases} \frac{P}{P^*} = (1 + m_p) \xi_p \left(\frac{v_p}{v^*}\right)^{m_p} \\ \begin{cases} P^* = K A^* = K W B \left(1 - \frac{a}{W}\right)^{m_1} \left[\arctan\left(b_1 \frac{B}{W}\right) + b_2 \right]^{m_2} \\ v^* = W \\ \xi_p = \frac{n k_1 k_3^{1/n+1}}{n+1} \\ m_p = \frac{k_4}{n} + k_4 + k_2 - 1 \end{cases} \end{cases} \quad (19)$$

where A^* is the characteristic area, given by $A^* = V^*/v^*$, and P^* is the characteristic load associated with geometric dimensions. Equation (19) outlines the dimensionless plastic load–displacement model for specimens with mode I cracks under 3D constraints (abbreviated as the CS- $p\nu$ model).

Table 1 Details of the finite element model for CT and SEB specimens

Model	Element models	Configuration sizes	Node counts	Element counts	
		$W = 50 \text{ mm}$ $a/W = 0.5, 0.6, 0.7, 0.8, B/W = 0.1, 0.3, 0.5, 0.7, 1.5, 3, 6$	29,533 ($a/W = 0.5, B/W = 0.5$)	24,438 ($a/W = 0.5, B/W = 0.5$)	
				27,503 ($a/W = 0.6, B/W = 1.5$)	22,758 ($a/W = 0.6, B/W = 1.5$)
				25,473 ($a/W = 0.7, B/W = 6$)	21,078 ($a/W = 0.7, B/W = 6$)
				23,443 ($a/W = 0.8, B/W = 0.1$)	19,398 ($a/W = 0.8, B/W = 0.1$)
		$W = 20 \text{ mm}$ $a/W = 0.5, 0.6, 0.7, 0.8, B/W = 0.1, 0.25, 0.5, 0.75, 1.5, 3, 6$	13,608 ($a/W = 0.5, B/W = 0.25$)	11,304 ($a/W = 0.5, B/W = 0.25$)	
				13,146 ($a/W = 0.6, B/W = 0.5$)	10,920 ($a/W = 0.6, B/W = 0.5$)
				12,684 ($a/W = 0.7, B/W = 0.75$)	10,536 ($a/W = 0.7, B/W = 0.75$)
				12,222 ($a/W = 0.8, B/W = 3$)	10,152 ($a/W = 0.8, B/W = 3$)

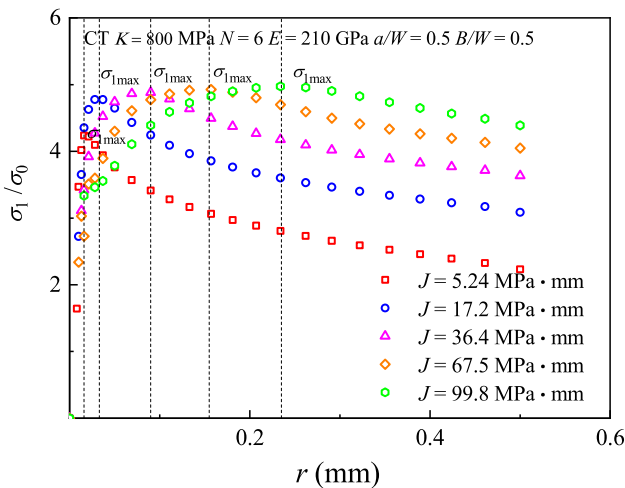


Fig. 1 Distribution of crack tip first principal stress

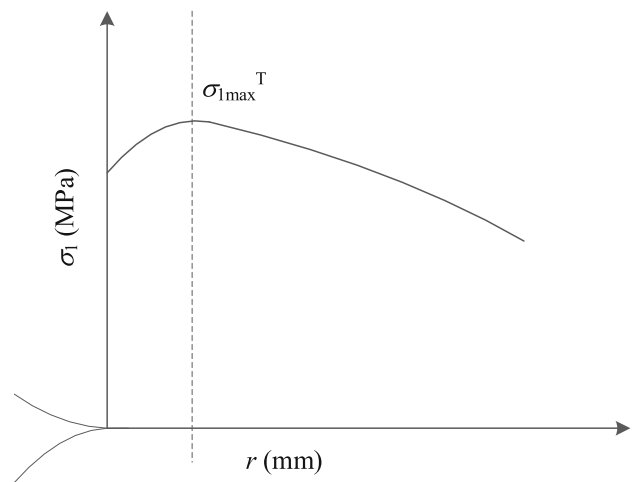


Fig. 2 Schematic diagram of maximal first principal stress σ_{1max}^T

3 Maximal Principal Stress Model at Mode I Crack Tip

3.1 FEA of Specimens with Mode I Cracks

Compact tension (CT) and single-edge notch-bending (SEB) specimens were selected as typical mode-I-cracked specimens to investigate crack tip stress fields. Their deformation

processes were analyzed under 3D large deformation conditions using the finite element software ANSYS 14.5. Solid 185 elements were utilized to develop quarter models of the CT and SEB specimens. The meshes at crack tips were locally refined, and the selected mesh density was not sensitive to the calculated results. Table 1 summarizes the details of CT and SEB models, with red shaded faces in both models indicating symmetric constraints applied during calculations.

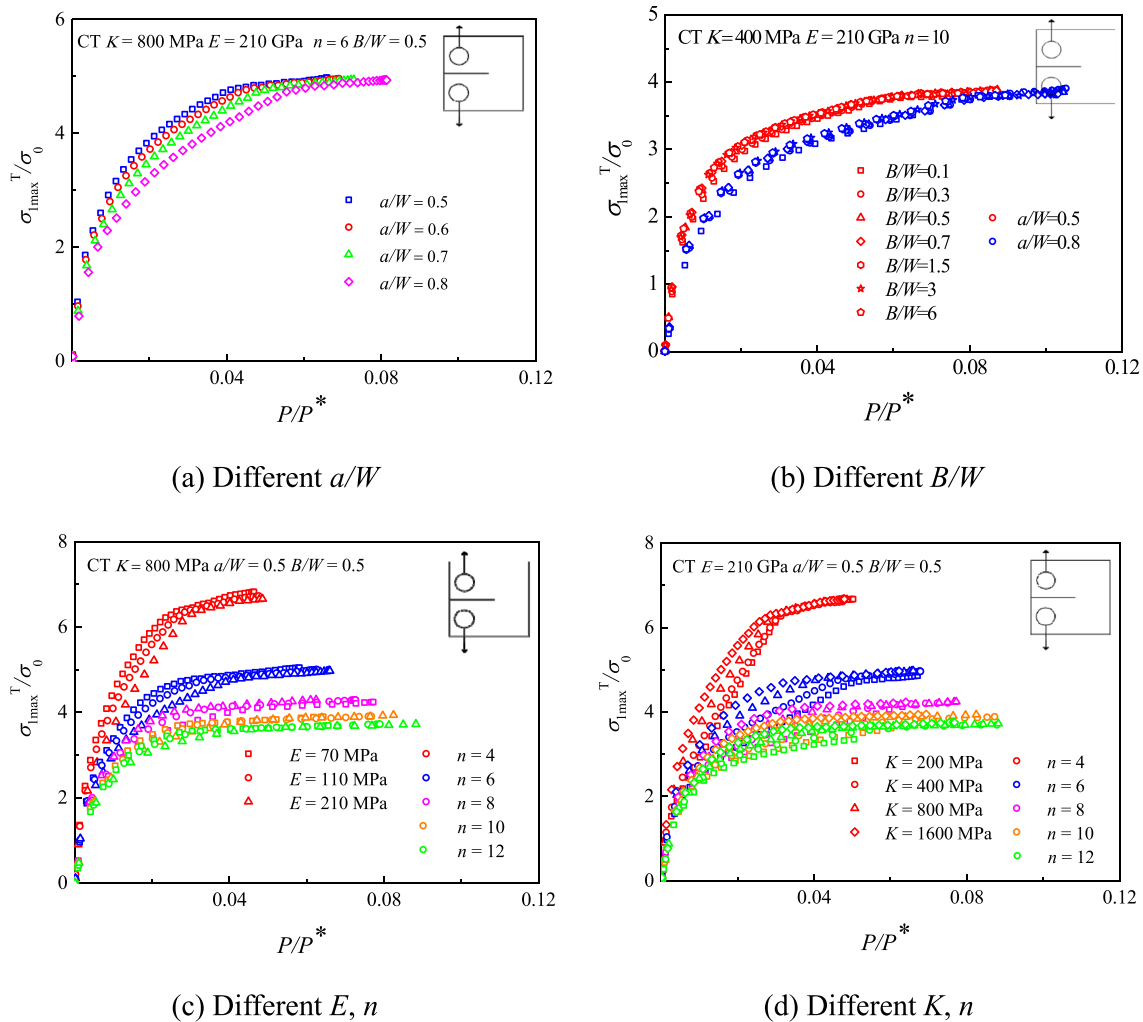


Fig. 3 $\sigma_{1\max}^T/\sigma_0$ - P/P^* curves of CT specimens

3.2 Distribution and Evolution of Crack-Tip First Principal Stress

Studies on ductile material critical fracture behaviors in [24, 25] have identified the primary controlling parameter of ductile fracture as the first principal stress. Accurate description of the maximal crack tip first principal stress is essential for predicting the onset of mode I cracks using the stress fracture criterion. Numerous experiments [30–32] have demonstrated that crack initiation occurs at the crack tip on a surface with symmetric thickness. FEA was used to determine the distribution of the first principal stress in the crack tip region where the crack surface and symmetric thickness surface meet.

A CT specimen was employed as an example to show the distribution of the first principal stress at the intersection line between the crack surface and the symmetric thickness surface under different loads. The constitutive parameters of the CT specimen were $K = 800$ MPa, $E = 210$ GPa, and $n = 6$, and its geometric parameters were $a/W = 0.5$ and

$B/W = 0.5$. The obtained results are displayed in Fig. 1. The material yield stress, denoted as σ_0 , was obtained from stress–strain curves to normalize the first principal stress. It was observed that the first principal stress distribution first increased and then decreased in the crack tip region, with the maximal first principal stress point gradually moving away from the crack tip with increasing load. In Fig. 2, the first principal stress at the maximal point was denoted as $\sigma_{1\max}^T$. When the relationship between the first principal stress and stress triaxiality at the maximal principal stress point satisfied the ductile material critical fracture criterion [24, 25], crack initiation occurred.

Establishing a dimensionless relationship between the maximal first principal stress and the load ($\sigma_{1\max}^T/\sigma_0$ - P/P^*) during the loading process is crucial to pinpoint mode I crack initiation under 3D constraints. Large-deformation FEA was applied to obtain $\sigma_{1\max}^T/\sigma_0$ - P/P^* curves of CT and SEB specimens with various materials and geometric dimensions.

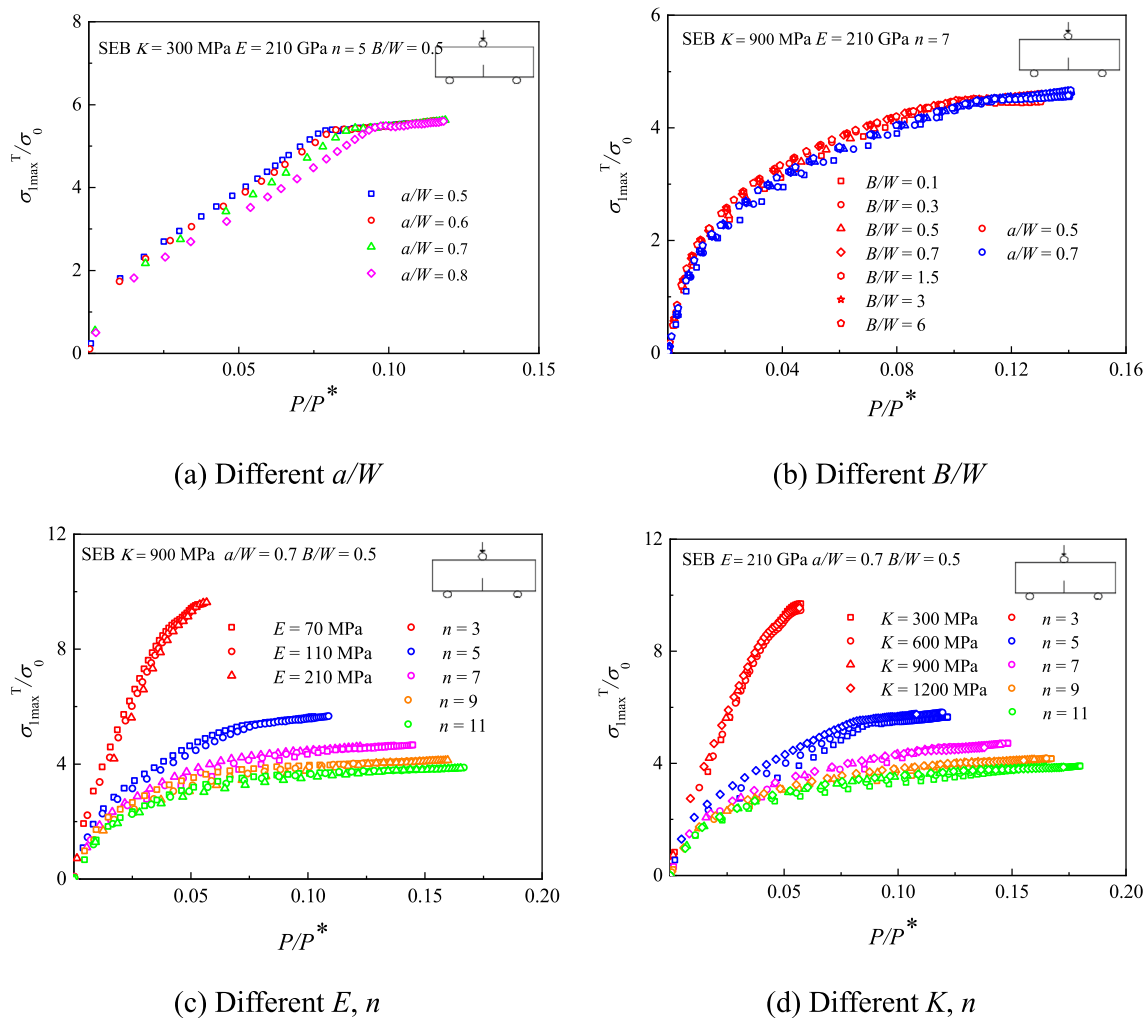


Fig. 4 $\sigma_{1max}^T/\sigma_0-P/P^*$ curves of SEB specimens

The results are illustrated in Figs. 3–4. The $\sigma_{1max}^T/\sigma_0-P/P^*$ curves reveal the following rules:

- (1) For all specimens with various materials and geometries, the trend of $\sigma_{1max}^T/\sigma_0-P/P^*$ curves evolved in the following manner: Initially, there was a significant increase in σ_{1max}^T/σ_0 as P/P^* rose, marking the ascending period. Once the specimens underwent a certain degree of elastic–plastic deformation, σ_{1max}^T/σ_0 stabilized, showing no significant change with further increases in P/P^* , indicating the onset of the stable period.
- (2) Figs. 3a and 4a indicated that as crack length a/W increased from 0.5 to 0.8, the value of σ_{1max}^T/σ_0 under the same P/P^* significantly decreased during the ascending period, while remaining relatively constant during the stable period.
- (3) Figs. 3b and 4b demonstrated a slight change in $\sigma_{1max}^T/\sigma_0-P/P^*$ curves for specimens with mode I

- cracks of varying B/W ratios. This slight change must be carefully investigated because thickness parameters significantly influenced crack initiation. Among specimens with different B/W ratios, those with values of 0.1 and 6 determined the minimal and maximal σ_{1max}^T/σ_0 values under the same P/P^* , respectively.
- (4) Figs. 3c, d and 4c, d showed the influences of material parameters K , E , and n on $\sigma_{1max}^T/\sigma_0-P/P^*$ curves. The ascending periods of $\sigma_{1max}^T/\sigma_0-P/P^*$ curves exhibited clear correlations with K , E , and n , while the stable periods were only closely related to n .

3.3 Description Model for Crack-Tip Maximal First Principal Stress

To accurately describe the dimensionless relationship between the crack-tip maximal first principal stress and the load for specimens with mode I cracks under 3D constraints,

Table 2 Parameters of the description model for maximal first principal stress

	m_1	m_2	b_1	b_2	k_1	k_2	k_3	k_4
	2.135	0.820	2.00	3.20	0.336	0.00882	0.477	0.991
CT	p_1	p_2	p_3	p_4	p_5	p_6		
	0.0362	6.71	0.0504	0.149	0.0451	-0.0239		
	p_7	p_8	p_9	p_{10}	p_{11}			
	-0.217	-0.757	6.51×10^{-13}	170	-5.04			
	m_1	m_2	b_1	b_2	k_1	k_2	k_3	k_4
	1.95	0.400	2.00	1.00	0.687	0.000101	0.375	0.980
SEB	p_1	p_2	p_3	p_4	p_5	p_6		
	-9.28×10^{-5}	8.97	0.0309	0.0385	-0.00248	-15.4		
	p_7	p_8	p_9	p_{10}	p_{11}			
	-0.0867	0.612	1.71×10^{-8}	95.2	-4.18			

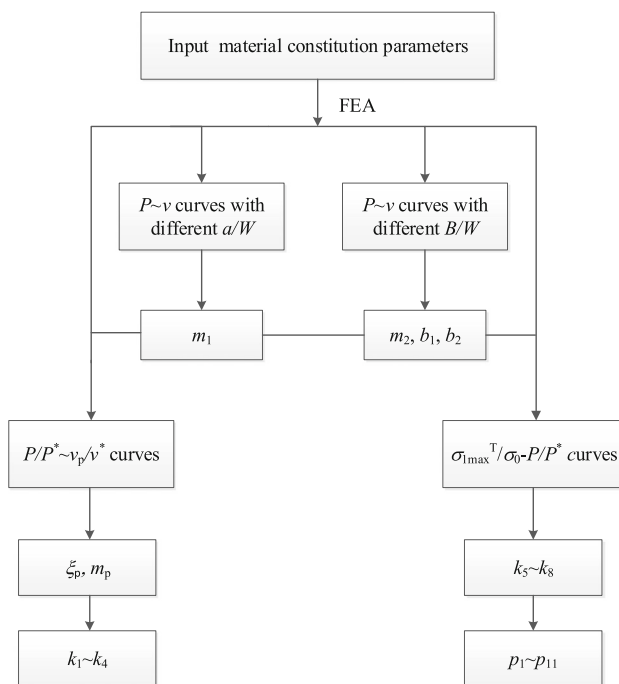


Fig. 5 Flow diagram of model parameter determination

all influencing factors, including geometric dimensions a/W , B/W , and material parameters K , E , and n , needed consideration.

The crack-tip maximal first principal stress $\sigma_{1\max}^T$ exhibited a positive relationship with the load and displacement of specimens with mode I cracks. Following the principle of dimensional analysis, the stress similarity criterion π_1 , load similarity criterion π_2 , and pure plastic displacement

similarity criterion π_3 are defined as

$$\begin{cases} \pi_1 = \frac{\sigma_{1\max}^T}{\sigma_0} \\ \pi_2 = \frac{P}{P^*} \\ \pi_3 = \frac{v_p}{v^*} \end{cases} \quad (20)$$

The relationship between π_1 , π_2 , and π_3 is stated as

$$\pi_1 = k_5 \pi_2 \pi_3^{k_6} + k_7 \pi_2 \pi_3^{k_8} \quad (21)$$

where k_5 and k_6 are parameters in the ascending periods of $\sigma_{1\max}^T/\sigma_0-P/P^*$ curves, associated with a/W , B/W , K , E , and n , while k_7 and k_8 pertain to the stable period of $\sigma_{1\max}^T/\sigma_0-P/P^*$ curves only associated with n .

From Eqs. (20) and (21), it can be deduced that

$$\frac{\sigma_{1\max}^T}{\sigma_0} = k_5 \frac{P}{P^*} \left(\frac{v_p}{v^*}\right)^{k_6} + k_7 \frac{P}{P^*} \left(\frac{v_p}{v^*}\right)^{k_8} \quad (22)$$

The parameters k_5 to k_8 were defined through the large-deformation FEA of various geometries and materials of specimens with mode I cracks.

By substituting the CS- p_v model from Eq. (19) into Eq. (22), the dimensionless relationship between the crack-tip maximal principal stress and the load can be obtained

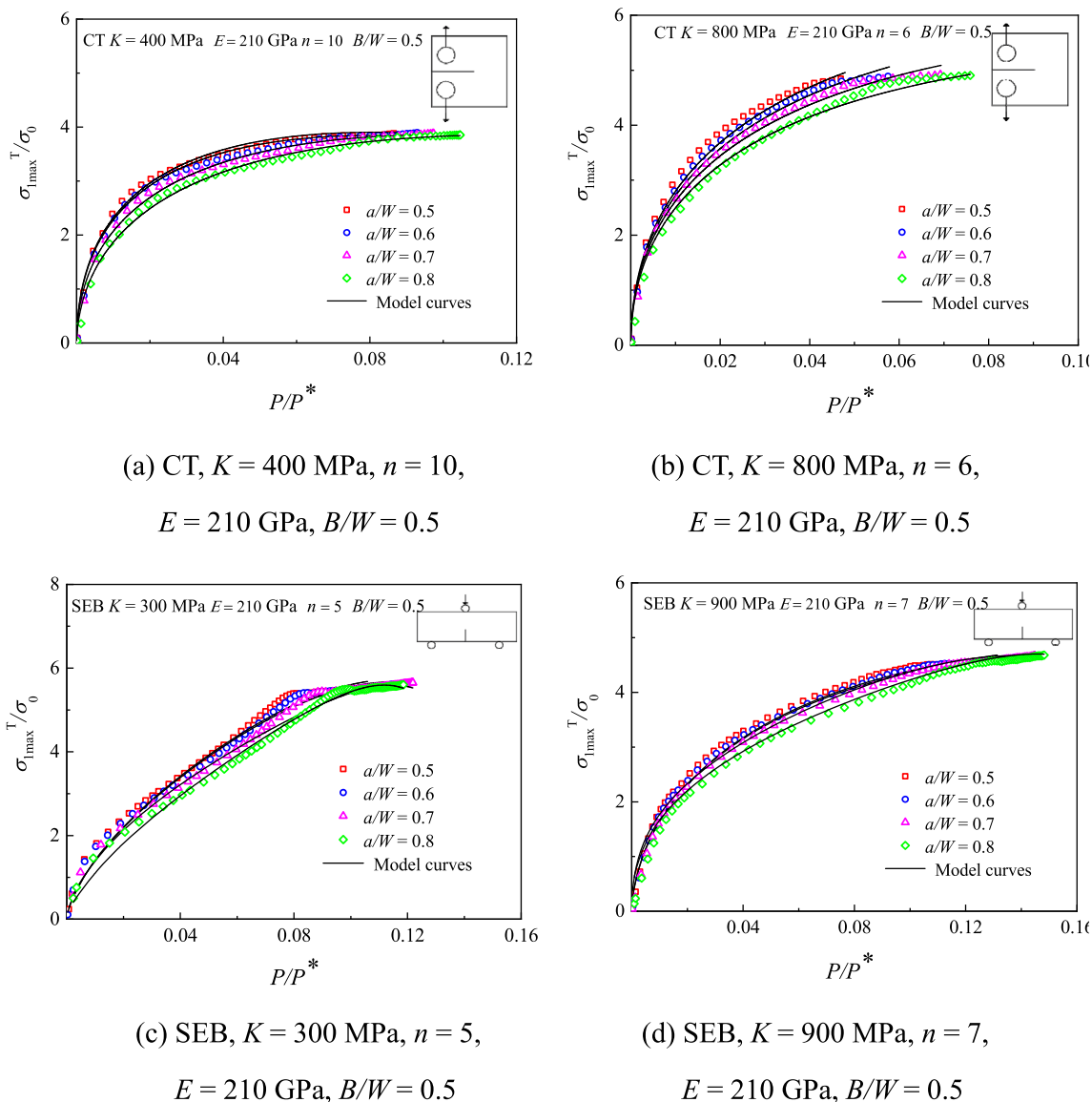


Fig. 6 $\sigma_{1\max}^T/\sigma_0$ - P/P^* curves with different a/W

as

$$\left\{ \begin{aligned} \frac{\sigma_{1\max}^T}{\sigma_0} &= k_5 \left[\frac{1}{(1+m_p)\xi_p} \right]^{\frac{k_6}{m_p}} \left(\frac{P}{P^*} \right)^{\frac{k_6}{m_p} + 1} \\ &+ k_7 \left[\frac{1}{(1+m_p)\xi_p} \right]^{\frac{k_8}{m_p}} \left(\frac{P}{P^*} \right)^{\frac{k_8}{m_p} + 1} \\ k_5 &= p_1 e^{p_2(\frac{1}{n+1} + 1)} \left(\frac{K}{E} \right)^{p_3(\frac{1}{n+1} + 1)} \left(1 - \frac{a}{W} \right)^{p_4} \\ &\quad \left(\left[\arctan\left(b_1 \frac{B}{W} \right) + b_2 \right]^{p_5} + p_6 \right) \\ k_6 &= p_7 \left(\frac{K}{E} \right) + \frac{p_8}{n+1} \\ k_7 &= p_9 \left(1 + \frac{1}{n+1} \right)^{p_{10}} \\ k_8 &= 1 + \frac{p_{11}}{n+1} \end{aligned} \right. \quad (23)$$

Equation (23) is referred to as the description model for the maximal first principal stress in specimens with mode I cracks (abbreviated as the CS- $\sigma_{1\max}^T$ model). The parameters p_1 to p_{11} can be determined through fitting calculations. Moreover, the CS- $\sigma_{1\max}^T$ model can be universally applied across various materials and geometric dimensions.

4 Validation of the Description Model for Maximal Principal Stress

4.1 Model Parameter Determination

The CS- $\sigma_{1\max}^T$ model is a mathematical equation with universal applicability and adheres to dimensional analysis.

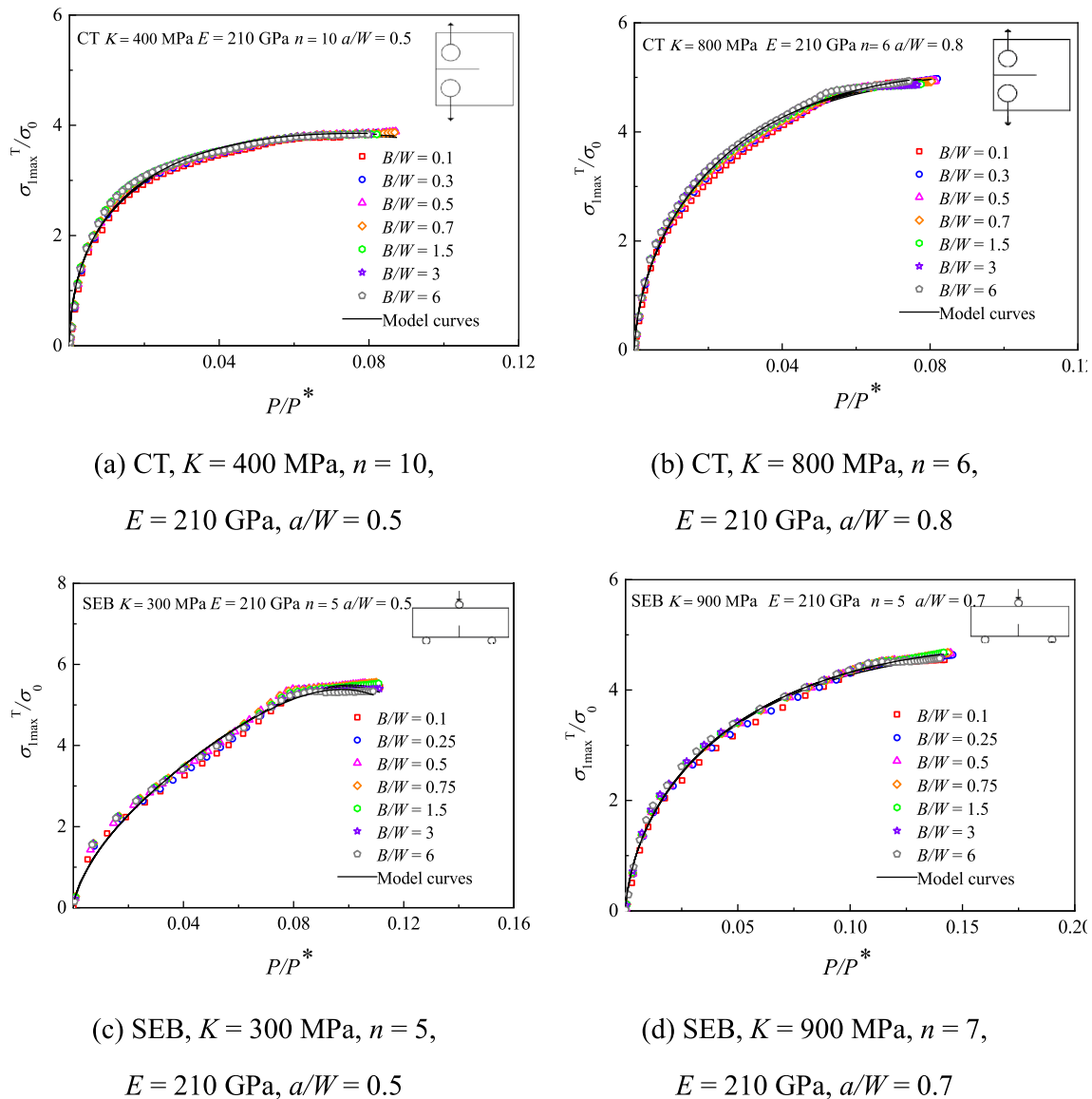


Fig. 7 σ_{1max}^T/σ_0 - P/P^* curves with different B/W

Model parameters, including k_1 to k_4 , m_1 , m_2 , b_1 , and b_2 , can be obtained through FEA, while p_1 to p_{11} are determined by fitting simulated data for different materials and geometries. Figure 5 illustrates the accurate parameter determination process. Table 2 outlines the parameter values for CT and SEB specimens.

4.2 Validation of CS- σ_{1max}^T Model

CT and SEB specimens of various materials and geometric dimensions were tested. For CT specimens, material parameters were $K = 200, 400, 600$, and 800 MPa, $E = 70, 110$, and 210 GPa, and $n = 4, 6, 8, 10$, and 12 , and geometric

parameters were $a/W = 0.5, 0.6, 0.7$, and 0.8 and $B/W = 0.1, 0.3, 0.5, 0.7, 1.5, 3$, and 6 . For SEB specimens, material parameters were $K = 300, 600, 900$, and 1200 MPa, $E = 70, 110$, and 210 GPa, and $n = 3, 5, 7, 9$, and 11 , and geometric parameters were $a/W = 0.5, 0.6, 0.7$, and 0.8 and $B/W = 0.1, 0.25, 0.5, 0.75, 1.5, 3$, and 6 . The calculations encompassed over 100 working conditions.

The σ_{1max}^T/σ_0 - P/P^* curves corresponding to these working conditions were obtained through FEA and compared with the prediction results from the CS- σ_{1max}^T model, as presented in Figs. 6, 7, 8, 9, 10. The σ_{1max}^T/σ_0 - P/P^* curves presented good consistency with the results derived using

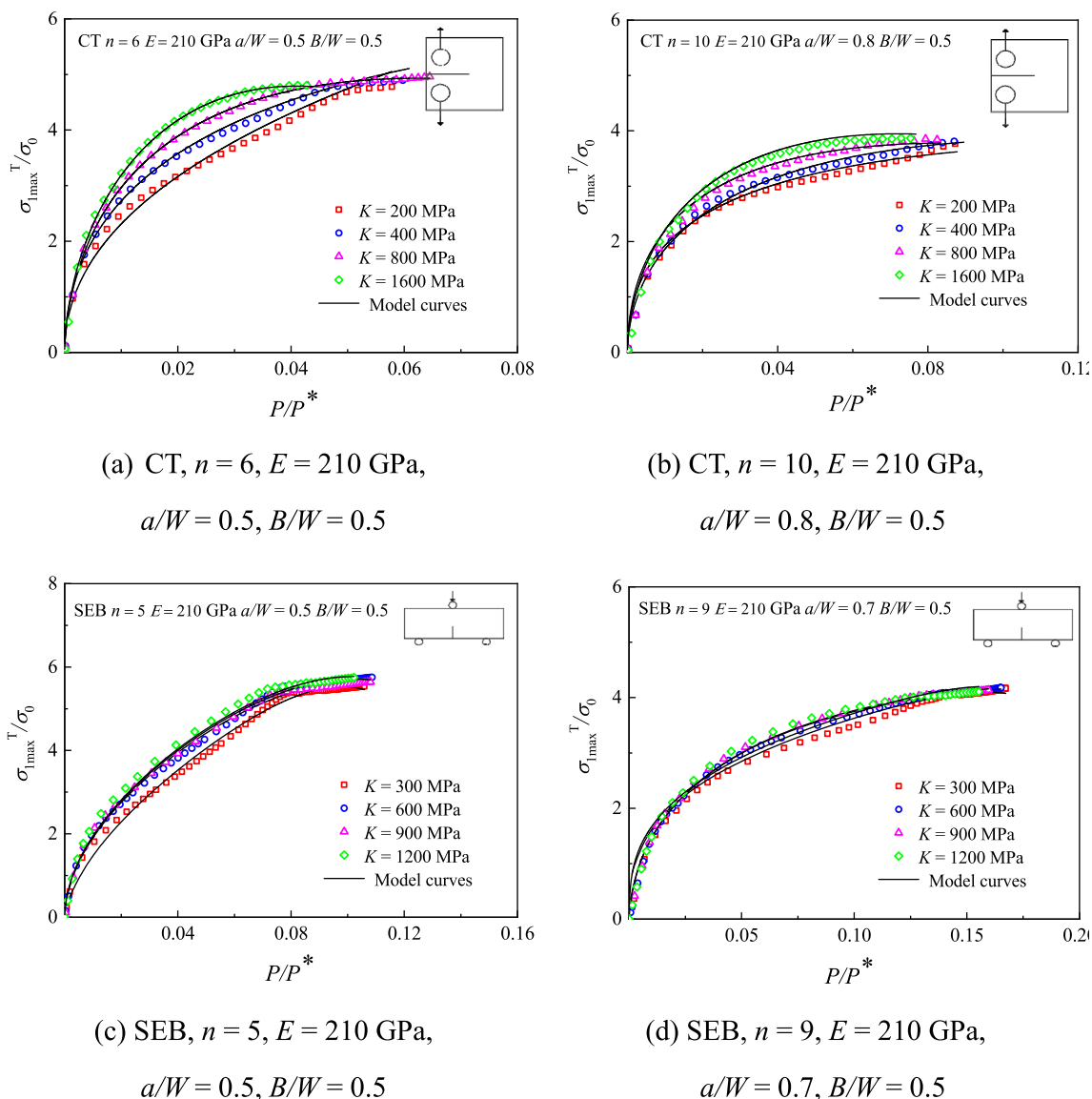


Fig. 8 $\sigma_{1max}^T/\sigma_0-P/P^*$ curves with different K

the CS- σ_{1max}^T model under all conditions for both CT and SEB specimens, irrespective of variations in a/W , B/W , K , E , or n . This validated the ability of the CS- σ_{1max}^T model to accurately describe the dimensionless relationship between crack-tip maximal first principal stress and load across diverse materials and geometries.

5 Conclusions

The research examined the correlations between load, displacement, and maximal first principal stress at crack tips of specimens with mode I cracks under 3D constraints, with constitutive relationships conforming to the R-O law. The following conclusions were drawn:

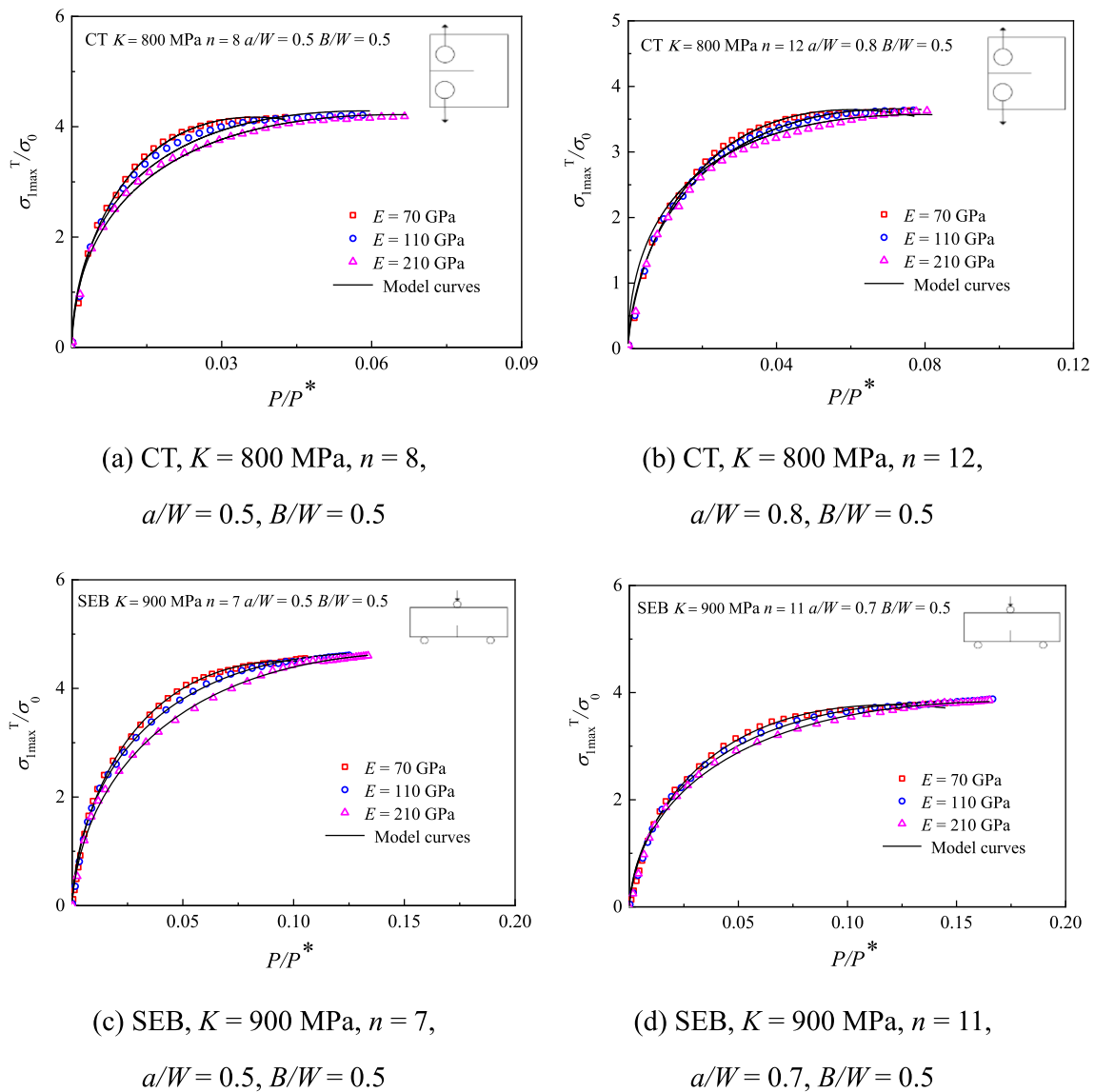
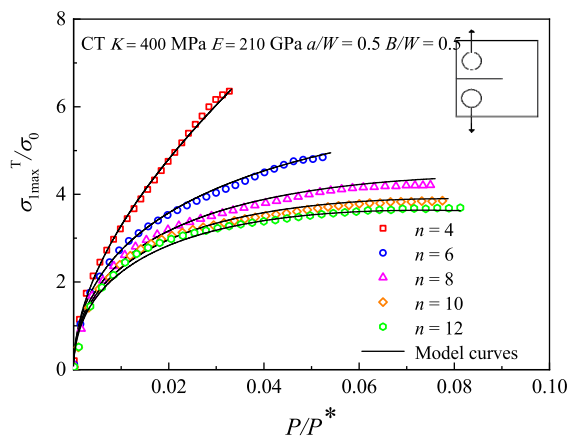
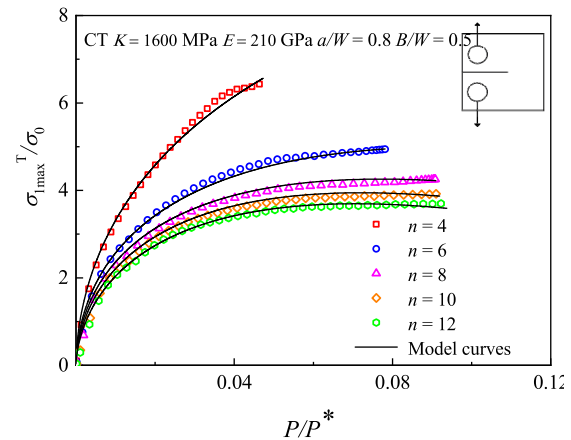


Fig. 9 $\sigma_{1\max}^T/\sigma_0$ - P/P^* curves with different E

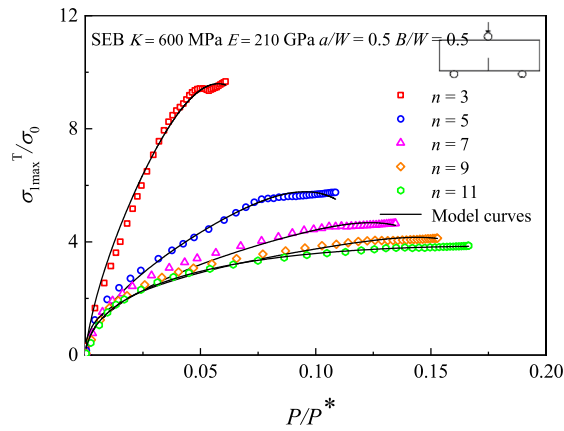
- (1) According to energy density equivalence and dimensional analysis, a CS- pv model was developed to characterize the dimensionless relationship between plastic displacement and load for specimens with mode I cracks under 3D constraints, considering the universality of materials and geometric dimensions .
- (2) The effects of constitutive and geometric parameters on dimensional relationships between the maximal first principal stress and the load were analyzed through large-deformation finite element analyses. The ascending periods of $\sigma_{1\max}^T/\sigma_0$ - P/P^* curves exhibited obvious correlations with all parameters a/W , B/W , K , E , and n . In contrast, the stable periods of the curves were only closely related to n .



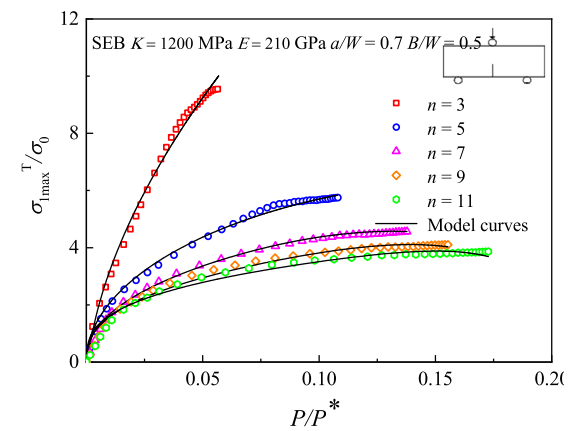
(a) CT, $K = 400$ MPa, $E = 210$ GPa,
 $a/W = 0.5$, $B/W = 0.5$



(b) CT, $K = 1600$ MPa, $E = 210$ GPa,
 $a/W = 0.8$, $B/W = 0.5$



(c) SEB, $K = 600$ MPa, $E = 210$ GPa,
 $a/W = 0.5$, $B/W = 0.5$



(d) SEB, $K = 1200$ MPa, $E = 210$ GPa,
 $a/W = 0.7$, $B/W = 0.5$

Fig. 10 $\sigma_{1\max}^T/\sigma_0-P/P^*$ curves with different n

(3) A CS- $\sigma_{1\max}^T$ model was developed to describe the dimensionless relationship between the crack-tip maximal first principal stress and the load. The effects of geometric parameters a/W and B/W , as well as constitutive parameters K , E , and n on $\sigma_{1\max}^T/\sigma_0-P/P^*$ curves were all taken into consideration.

(4) The CS- $\sigma_{1\max}^T$ model was validated through large-deformation finite element analyses under over 100 different working conditions. The predicted $\sigma_{1\max}^T/\sigma_0-P/P^*$ curves using the developed model agreed well with finite element results for CT and SEB specimens comprising various materials and geometries.

Acknowledgements This work is financially supported by the National Natural Science Foundation of China (Grant No. 11872320) and Sichuan Province Science and Technology Support Program (Grant No. 2023NSFSC1296).

References

- Westergaard HMW. Bearing pressures and cracks. *J Appl Mech.* 1939;6:A49–53.
- Williams ML. On the stress distribution at the base of a stationary crack. *J Appl Mech.* 1957;24(1):109–14.
- Irwin GR. Analysis of stresses and strains near the end of a crack traversing a plate. *J Appl Mech.* 1957;24(3):361–4.
- Cotterell B, Rice JR. Slightly curved or kinked cracks. *Int J Fracture.* 1980;16(2):155–69.
- Pham VB, Bahr HA, Bahr U, et al. Crack paths and the problem of global directional stability. *Int J Fracture.* 2006;141(3–4):513–34.
- Hello G, Tahar MB, Roelandt JM. Analytical determination of coefficients in crack-tip stress expansions for a finite crack in an infinite plane medium. *Int J Solids Struct.* 2012;49(3–4):556–66.
- Berto F, Lazzarin P. Multi-parametric full-field representations of the in-plane stress fields ahead of cracked components under mixed mode loading. *Int J Fatigue.* 2013;46:16–26.
- Stepanova L, Roslyakov P. Multi-parameter description of the crack-tip stress field: analytic determination of coefficients of crack-tip stress expansions in the vicinity of the crack tips of two finite cracks in an infinite plane medium. *Int J Solids Struct.* 2016;100–101:11–28.
- Cherepanov GP. Crack propagation in continuous media. *J Appl Math Mech.* 1967;31(3):503–12.
- Rice JR. A path independent integral and the approximate analysis of strain concentration by notches and cracks. *J Appl Mech.* 1968;35(2):379–86.
- Hutchinson JW. Singular behavior at the end of a tensile crack in a hardening material. *J Mech Phys Solids.* 1968;16(1):13–31.
- Rice JR, Rosengren GF. Plane strain deformation near a crack tip in a power-law hardening material. *J Mech Phys Solids.* 1968;16(1):1–12.
- O'Dowd NP, Shih CF. Family of crack-tip fields characterized by triaxiality parameter. *J Mech Phys Solids.* 1991;39(8):989–1015.
- O'Dowd NP, Shih CF. Family of crack-tip fields characterized by a triaxiality parameter-II. *Fracture Appl J Mech Phys Solids.* 1992;40:939–63.
- Joyce JA, Link RE. Application of two parameter elastic-plastic fracture mechanics to analysis of structures. *Eng Fract Mech.* 1997;57(4):431–46.
- Yang S, Chao YJ, Sutton MA. Higher order asymptotic crack tip fields in a power-law hardening material. *Eng Fract Mech.* 1993;45(1):1–20.
- Chao YJ, Yang S, Sutton MA. On the fracture of solids characterized by one or two parameters: theory and practice. *J Mech Phys Solids.* 1994;42(4):629–47.
- Nikishkov GP. Prediction of fracture toughness dependence on constraint parameter a using the weakest link model. *Eng Fract Mech.* 2016;152:193–200.
- Nikishkov GP, Matvienko YG. Elastic-plastic constraint parameter a for test specimens with thickness variation. *Fatigue Fract Eng M.* 2016;39:939–49.
- Matvienko YG, Nikishkov GP. Two-parameter J - A concept in connection with crack-tip constraint. *Theor Appl Fract Mec.* 2017;92:306–17.
- Withers PJ. Fracture mechanics by three-dimensional crack-tip synchrotron X-ray microscopy. *Philos T R Soc A.* 2015;373(2036):20130157.
- Sutton MA, Turner JL, Chao YJ, Bruck HA, Chae TL. Experimental investigations of three-dimensional effects near a crack tip using computer vision. *Int J Fracture.* 1992;53(3):201–28.
- Srilakshmi R, Ramji M, Chinthapenta V. Fatigue crack growth study of CFRP patch repaired Al 2024-T3 panel having an inclined center crack using FEA and DIC. *Eng Fract Mech.* 2015;134:182–201.
- Yu SM, Cai LX, Yao D, Bao C. Critical ductile fracture criterion based on first principal stress and stress triaxiality. *Theor Appl Fract Mec.* 2020;109: 102696.
- Yao D, Cai L, Bao C. A new fracture criterion for ductile materials based on a finite element aided testing method. *Mat Sci Eng A.* 2016;673:633–47.
- Chen H, Cai LX. Unified elastoplastic model based on a strain energy equivalence principle. *Appl Math Model.* 2017;52:664–71.
- Chen H, Cai LX. An elastoplastic energy model for predicting the deformation behaviors of various structure components. *Appl Math Model.* 2019;68:405–21.
- Chen H, Cai LX, Bao C. Equivalent-energy indentation method to predict the tensile properties of light alloys. *Mater Design.* 2019;162:322–30.
- Sharobeam MH, Landes JD. The load separation criterion and methodology in ductile fracture mechanics. *Int J Fracture.* 1991;47(2):81–104.
- ASTM E1820. Standard test method for measurement of fracture toughness. 2011.
- ISO 12135. Metallic materials—unified method of test for the determination of quasistatic fracture toughness. International Standard Organization; 2016.
- GB/T 21143. Uniform test method for quasi-static fracture toughness of metallic materials. 2014.

Springer Nature or its licensor (e.g. a society or other partner) holds exclusive rights to this article under a publishing agreement with the author(s) or other rightsholder(s); author self-archiving of the accepted manuscript version of this article is solely governed by the terms of such publishing agreement and applicable law.